Evaluation of an inverse modelling methodology for the prediction of a stationary point pollutant source in complex urban environments

George C. Efthimiou[a1], Ivan V. Kovalets[b], Christos D. Argyropoulos[c], Alexandros Venetsanos[a], Spyros Andronopoulos[a] and Konstantinos E. Kakosimos[c]

[a]Environmental Research Laboratory, INRASTES, NCSR Demokritos, Patriarchou Grigoriou & Neapoleos Str., 15310, Aghia Paraskevi, Greece

[b]Department of Environmental Informatics, Institute of Mathematical Machines and Systems Problems, National Academy of Sciences of Ukraine, Kiev, Ukraine

[c]Department of Chemical Engineering & Mary Kay 'O Connor Process Safety Center, Texas A&M University at Qatar, Education City, Doha, Qatar, PO Box 23874

Abstract

The estimation of a hazardous contaminant unknown source characteristics (i.e., rate and location) in a complex urban environment using efficient inverse modelling techniques is a challenging problem that involves advanced computational fluid dynamics combined with appropriate mathematical algorithms. In this paper we further assess our recently proposed inverse source term estimation method (Efthimiou et al., 2017, Atmos. Environ., 170, 118-129) by applying it in two wind tunnel experiments simulating atmospheric flow and tracer dispersion following a stationary release in realistic urban settings, namely Michelstadt and Complex Urban Terrain Experiment (CUTE). The method appears to be robust and to predict with encouraging accuracy the source location and emission rate for both wind tunnel experiments.

Keywords: Inverse modelling; Source term estimation; CFD; ADREA-HF; Urban environment; Source inversion.

1. Introduction

In the event of a dangerous substance being released into the atmosphere, whether intentionally or by accident, the transport of the material as a wind-blown plume can distribute it over a large area and may pose threats to the populations in the course of the plume (Argyropoulos et al., 2010; Argyropoulos et al., 2013; Argyropoulos et al., 2017; Markatos et al., 2009; Nivolianitou et al., 2012). The Chernobyl (Anspaugh et al., 1988), and relatively recent Fukushima (Ohtsuru et al., 2015) nuclear disasters, the Sarin gas terrorist attacks in Matsumoto town (Morita et al., 1995) and Tokyo (Okumura et al., 1996) in Japan, as well as the well-known chemical accidents of Bhopal (Chouhan, 2005), and Seveso (Pocchiari et al., 1979) are significant events which caused severe environmental and human health and life consequences.

During an event of the type described above and if the source location, the release rate and type of pollutants are known, dispersion models can be used to forecast the plume trajectory of the air pollutants, their dispersion and eventual deposition as well as the level of human exposure to the pollutant(s) (Lioy et al, 2016). The necessary meteorological information may originate from local weather stations or may be forecast data provided by Numerical Weather Prediction models. If the source characteristics, such as location, release rate and pollutant type (collectively mentioned as

---

[1] Corresponding author. E-mail address: gefthimiou@ipta.demokritos.gr (G. C. Efthimiou).

"source term") are unknown and the only available information is readings at different locations and time intervals, the reconstruction of the source term of the airborne pollutant can usually be obtained by using forward or backward (inverse) modelling approaches, in combination with the existing measurements (Hutchinson et al., 2017; Rao, 2007).

Important research has been performed in developing methods for the identification of the unknown source of an airborne material. Various researchers have tried to combine inverse modelling techniques with the Computational Fluid Dynamics (CFD) (either RANS, Efthimiou et al., 2017 or LES, Mons et al., 2017). There are also research efforts in the literature to combine inverse modelling with Gaussian modelling (e.g. Ma and Zhang, 2016; Ma et al., 2017; Wang et al., 2017) and Lagrangian modelling (Zheng et al., 2007).

Dispersion in urban environment leads to additional difficulties in application of source term estimation (STE) algorithms because of strong concentration fluctuations (e.g. Efthimiou et al, 2016) due to the influence of 'inherently strong features of the flow field' (Blocken et al., 2011) and turbulence on plume dispersion. Some indicative examples of STE methods suitable for applications in urban environment are listed below. Ma and Zhang (2016) applied machine learning algorithms (MLA) along with three different gas dispersion models (i.e. CFD, Gaussian and Lagrangian Stochastic) for source identification problem and found that the best performance was exhibited for the Gaussian – Support Vector Machine (SVM) model. Mons et al. (2017) used a LES solver combined with data assimilation techniques to identify the wind parameters and contaminant source characteristics from observations of the concentration levels. Xue et al. (2017) used Bayesian inference for source term estimation in urban environment together with the estimation of the unknown Schmidt number and were able to show that adding Sc to the list of the unknown variables improved the results of STE algorithm. Xue et al. (2018) proposed a novel source term estimation method based on LES approach using Bayesian inference. The source-receptor relationship was obtained by solving the adjoint equations constructed using the time-averaged flow field simulated by the LES approach based on the gradient diffusion hypothesis. A wind tunnel experiment with a constant point source downwind of a single building model was used to evaluate the performance of the proposed method, which was compared with that of the existing method using a RANS model. The results showed that the proposed method reduced the errors in estimating the source location and the emission rate by 77% and 28% respectively (the location error is expressed as the Euclidian distance between the estimated and true source position and the emission rate error, as the ratio of estimated to true source strength). Kumar et al. (2015) described a methodology combining a renormalization inversion technique with a building-resolving CFD approach for source retrieval in the geometrically complex urban regions. The source parameters (i.e., source location and release rate) were reconstructed from a finite set of point measurements of concentration acquired from some sensors and the adjoint functions computed from the CFD model. The inversion procedure was evaluated for a point source reconstruction using measurements from the Mock Urban Setting Test (MUST) field experiment under various stability conditions. The results were encouraging. Kouichi et al. (2018) presented a methodology for the optimization of a monitoring network of sensors measuring the polluting substances in an urban environment with a view to estimate an unknown emission source. The methodology was presented by coupling the Simulated Annealing algorithm with the renormalization inversion technique and the CFD modeling approach. This approach was successfully applied and validated with 20 trials of the MUST tracer field experiment in an urban-like environment.

Recently, Efthimiou et al. (2017) exhibited an optimized inverse modelling method for the reconstruction of pollutant stationary source characteristics in urban environment. The method eliminates the 'overfitting' effect by determining the source location and rate separately, through a two-step segregated approach that combines a correlation coefficient and a cost function, instead of using a single cost function as was done previously by Kovalets et al. (2011). The method was recently extended by Kovalets et al., (2018) for the case of transient dispersion problem.

Efthimiou et al. (2017) obtained satisfactory results in predicting a stationary source location and rate in the case of the medium-complexity MUST wind tunnel experiment (similar building blocks arranged in regular rows). The purpose of the present paper is to investigate the robustness of the STE algorithm for the case of stationary source but more complex urban areas with arbitrarily arranged building blocks of various shapes and also more diverse source locations as compared to MUST experiment, such as source located in open squares, narrow or wide streets, etc. Based on our past experience with simulations of two complex and realistic urban environments (Efthimiou et al., 2015; Efthimiou et al., 2016; Efthimiou et al., 2018; Efthimiou et al., 2016), we selected the Michelstadt and the CUTE wind tunnel experiments for the further assessment of our inverse source estimation algorithm.

2. Methodology – Source term estimation algorithm

The first version of the inverse source term estimation algorithm was described by Kovalets et al., (2011) and the optimised version that is used in this paper has been described by Efthimiou et al., (2017). The outline and the basic relationships of the algorithm will be given here.

The basic assumptions of the problem are that there is a constant-in-time air flow field established over an urban area, into which a pollutant is emitted at a constant rate from a point source. The steady-state flow field is calculated by a Computational Fluid Dynamics (CFD) model. Besides the steady-state flow field, the only available information is concentration measurements at several sensors locations inside the urban area under consideration. The source can be located anywhere in the computational domain. The location of the source is estimated by calculating and finding the minimum of the following cost function:

$$J = -\frac{\left\langle \left(c^c - \left\langle c^c \right\rangle\right)\left(c^o - \left\langle c^o \right\rangle\right) \right\rangle}{\sqrt{\left\langle \left(c^c - \left\langle c^c \right\rangle\right)^2 \right\rangle}\sqrt{\left\langle \left(c^o - \left\langle c^o \right\rangle\right)^2 \right\rangle}} \tag{1}$$

where c^c indicates calculated and c^o indicates observed concentration respectively, both at the sensors locations and $\langle \ \rangle$ denotes arithmetic averaging over all sensors positions. The function J is minimized with respect to the source location, therefore the values of c^c must be calculated at each sensor for all potential source locations. This can be accomplished by solving the "forward"-in-time dispersion problem considering as source all potential source locations. However, in the cases examined in this paper the potential source locations are virtually infinite. Therefore, it is computationally more efficient to calculate the c^c's in an inverse mode, using the concept of the "Source-receptor functions" (SRFs) which describe the sensitivity of concentration at a receptor to the parameters of the emitting source. To this end, the adjoint form of the dispersion model is run using each time as source a sensor location. The differential — steady state — equation of the adjoint variable $c*$ is:

$$\frac{\partial c_n^*}{\partial t} - u_i \frac{\partial c_n^*}{\partial x_i} - \frac{\partial}{\partial x_i} D \frac{\partial c_n^*}{\partial x_i} = p_n \tag{2}$$

where n is the measurement point counter, p is the probing function (connecting the value at the measurement point with the value at the computational grid node where the variable is originally calculated), D is the coefficient of turbulent diffusion, u_i are the constant-in-time flow velocity

components in a Cartesian coordinate system with coordinates $x_i = (x, y, z)$, $i = 1–3$. As already mentioned, the latter are calculated by a CFD model. In the particular cases described in this paper a Reynolds-Averaged Navier-Stokes (RANS) model has been used, as will be discussed below. The values of D have also been calculated by the CFD model using the standard k-ε turbulence closure scheme (Argyropoulos and Markatos, 2015, Launder and Spalding, 1974). This turbulence model has been used giving reasonable results in several studies of wind flow and pollutant dispersion in complex urban environments (e.g., Trini Castelli et al., 2017, Pontiggia et al., 2010, Santiago et al., 2010, Wang et al., 2009, Flaherty et al., 2007, Hanna et al. 2006).

The nodes of the numerical grid that is used to spatially discretize and solve Equation (2) constitute the potential source locations. The calculated concentrations that enter cost function (1) are expressed by the SRF as $c^c = q^s\, c^*$, where q^s is an arbitrary source emission rate. Efthimiou et al. (2017) have shown that an arbitrary value for q^s can be used in the case of a stationary source of a passive and non-reactive tracer. With c^c 's calculated through the SRFs, the values of function J (Eq. 1) are calculated for all potential source locations (i.e., at all grid nodes) and their minimum indicates the estimated source location.

Having identified by the above procedure the grid node, k^s, where the source is located, the source emission rate is calculated from the following equation:

$$q^s = \frac{\sum_{n=1}^{K} c^*_{n,k^s} c^o_n}{\sum_{n=1}^{K} \left(c^*_{n,k^s} \right)^2} \tag{3}$$

where K is the number of sensors and c^*_{n,k^s} is the value of the adjoint variable from sensor n at the node k^s.

The method presented above has recently been extended by Kovalets et al. (2018), to deal with problems of transient pollutant dispersion under stationary meteorological fields, allowing for the identification of the location, start time, duration and quantity of emitted substance of an unknown air pollution source of finite time duration.

3. The wind tunnel experiments

3.1. The "Michelstadt" wind tunnel experiment

The "Michelstadt" wind tunnel experiment represents an idealized Central-European urban environment and has been extensively used in the past for model validation purposes (Efthimiou et al., 2016; Efthimiou et al., 2018; Baumann-Stanzer et al., 2015). The wind tunnel model had a geometric scale equal to 1:250. Flow and concentration measurements were performed at various locations and heights above ground. There were seven release scenarios corresponding to different point source locations (in open squares, narrow or wide streets, streets aligned perpendicular or parallel to the prevailing large-scale flow, courtyards) and two different incident wind directions (0° and 180°, Fig. 1). The reference velocity U_{ref} (at reference height 99.9 m) was equal to 6 ms^{-1}. Only cases with continuous releases of the tracer substance have been considered in the present study. More information about the experiment can be found in www.elizas.eu.
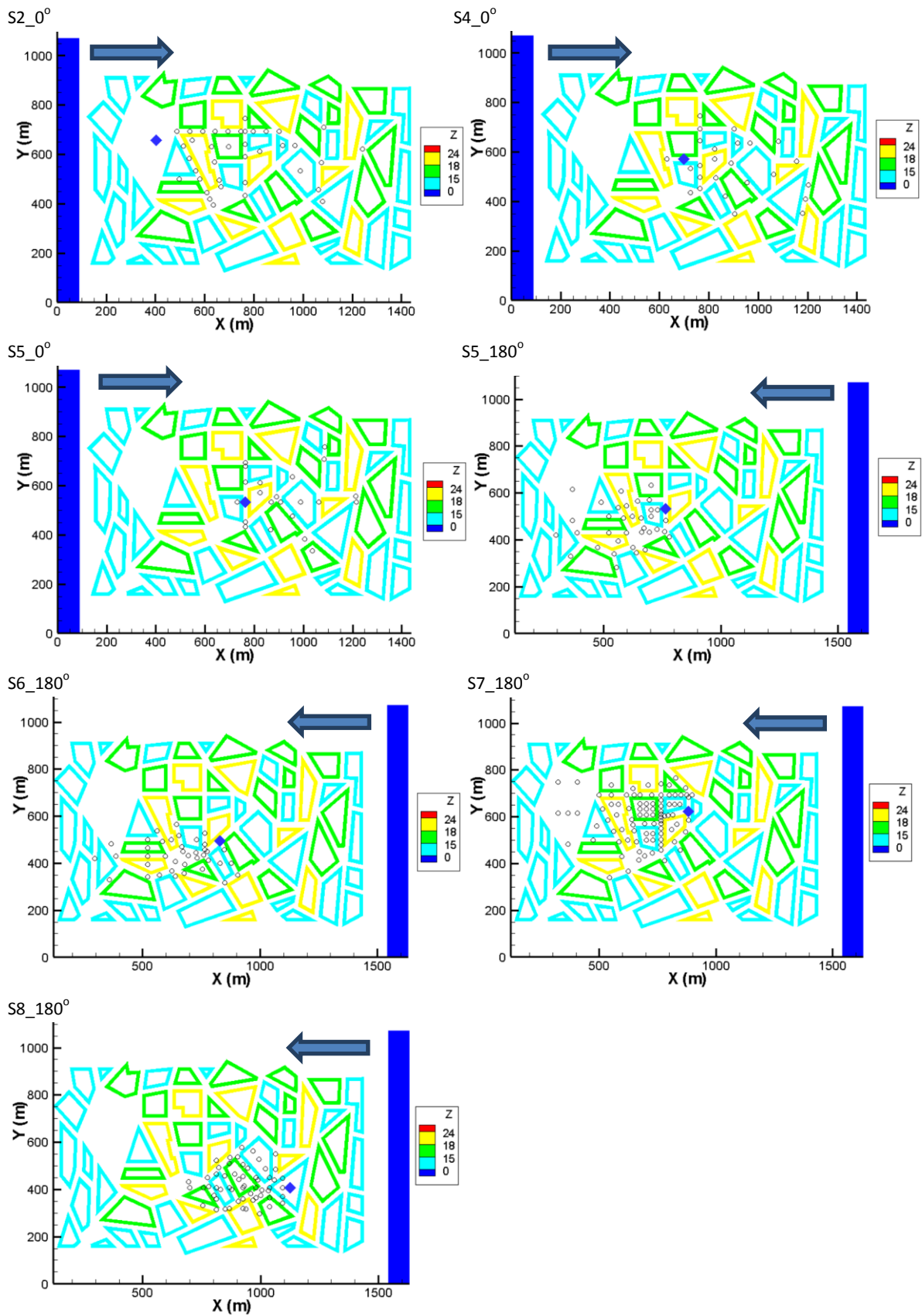
Figure 1: Source location (solid blue diamond), and receptor points (open circles), where concentration was measured for different cases of the Michelstadt experiments. The wind direction is from left to right for cases S2_0°, S4_0° and S5_0° and from right to left for cases S5_180°, S6_180°, S7_180° and S8_180°. z represents the building height while the arrow in each plot indicates the incident wind direction.

3.2. The Complex Urban Terrain Experiment (CUTE) wind tunnel experiment

The CUTE experiment was carried out to test atmospheric dispersion models with potential use in the wider context of emergency response related to accidental air pollution in urban areas (Baumann-Stanzer et al., 2015). The test site was the downtown area of a typical Central European city. The building heights were between 25 and 35 m. The wind tunnel model had a geometric scale equal to 1:350. The available information for the flow field of the CUTE wind tunnel dataset was limited to the wind speed and direction at a reference height (z_{ref} = 49 m). The wind direction was 235° (south-westerly winds) and the wind speed U (z_{ref}) was equal to 6 m/s. This strategy was adopted to test the dispersion model under realistic emergency conditions, where limited meteorological data would be available (possibly from 1 meteorological station). Therefore, wind velocity measurements were not available. Only tracer concentration data were available for model validation purposes. In the present paper, we used the data collected from "case 3" of the CUTE wind tunnel experiment. In the chosen case, the tracer gas was released at a steady rate from a point source located between houses near the river on the opposite side of the harbour (Figure 2). The concentration-time series were measured by 34 sensors which locations are shown in Figure 2. Besides the continuous release case considered in the present paper, puff release cases were also included in the series of the CUTE experiments. Such cases were considered by Kovalets et al. (2018).
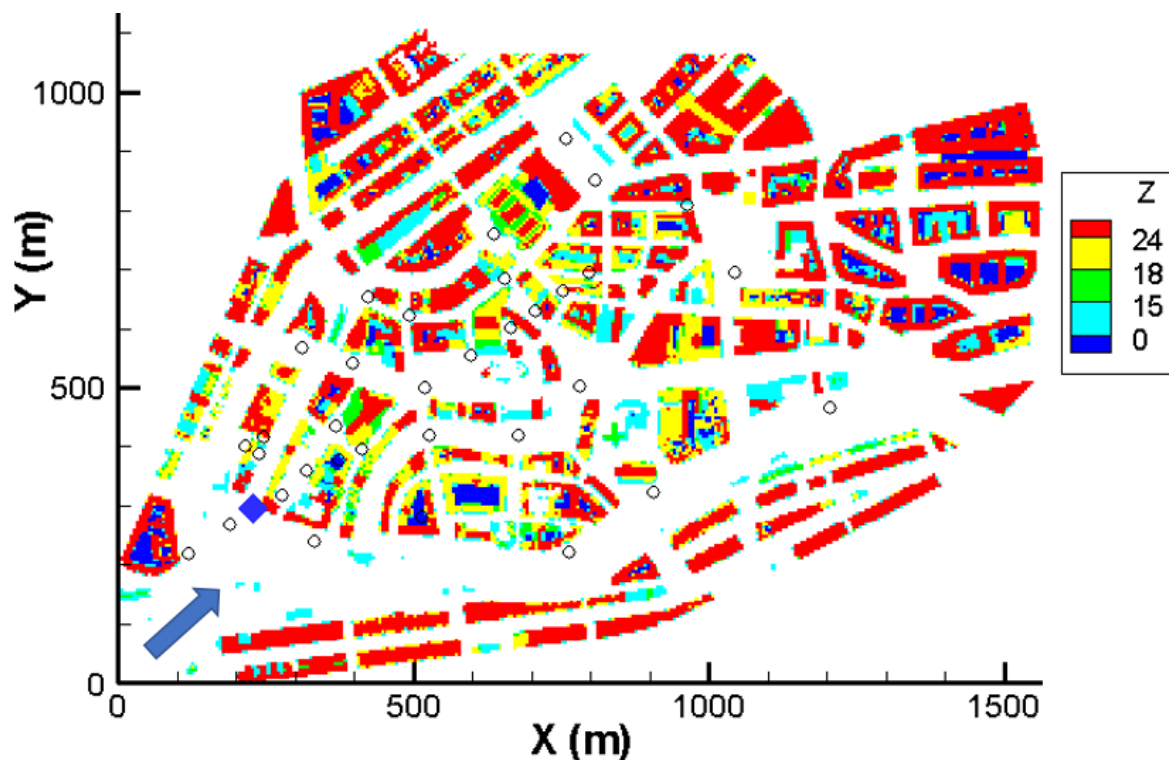

Figure 2: Source location (solid blue diamond), and receptor points (open circles), where concentration was measured for the CUTE experiment. z represents the building height while the arrow indicates the incident wind direction.

4. The numerical simulations

All computations (wind flow and adjoint dispersion modelling) were performed with the CFD code ADREA-HF (Bartzis 1991, Andronopoulos et al. 1994, Andronopoulos et al. 2002, Venetsanos et al. 2010). The Eulerian version of the model, solving the unsteady RANS equations has been used in this

study. The code uses finite volumes with rectangular parallelepiped cells for the discretization of the transport equations. To describe the complex geometry, the volume porosity concept is used with solid surfaces of any orientation allowed to cross the computational cells.

4.1. The wind field simulations

The computational domain dimensions and the numerical spatial discretizations used for the wind flow simulations of the two wind tunnel experiments are presented in Table 1. The grid used for the Michelstadt experiment was the result of a grid sensitivity study that was carried out to ensure that the present numerical solutions are grid-independent. The details of this analysis and the rationale for constructing the grid are presented in Appendix A. Based on this study, the minimum horizontal and vertical resolutions used for the CUTE experiment were set equal to those of the Michelstadt computations, i.e., $dx_{min} = dy_{min} = 3$m and $dz_{min} = 1$m, which resulted in a grid consisting of 12,419,792 cells (Table 1).

Table 1: Size of the selected computational domains and numerical grids.

Experiment	Domain dimensions $x/y/z$ (m)	Total number of cells	Number of cells in each axis			Minimum/maximum cell sizes (m)		
			x	y	z	x	y	z
Michelstadt	1800.05/1070.93/144	7,595,838	482	309	51	3.0/35.71	3.0/14.04	1.0/8.27
CUTE	3725.2/3375.02/648	12,419,792	593	476	44	3.0/150.57	3.0/150.57	1.0/59.69

For Michelstadt, the domain extends horizontally by 120 m (5 H_{max}, H_{max}=24 m being the maximum buildings height) upwind of the first buildings and by 360 m (15 H_{max}) downwind of the last buildings. The vertical dimension of the domain is about 6 H_{max}. For CUTE the domain extends horizontally by 540 m (5 H_{max}, H_{max}=108 m being the maximum buildings height) upwind of the first buildings and by 1620 m (15 H_{max}) downwind of the last buildings. The vertical dimension of the domain is about 6 H_{max}. The above dimensions conform to the recommendations of COST Action 732 (Franke et al., 2007).

The conservation equations solved for both experiments were those of mass and momentum. In addition, since for turbulence modelling, the standard k–ε model was adopted, the transport equations of turbulent kinetic energy and its dissipation rate were also solved. Neutral stability conditions have been assumed, therefore no temperature or energy equations were solved. The boundary conditions for the hydrodynamic variables at each boundary plane or solid surface of the domain are presented in Table 2.

Table 2: Boundary conditions for the hydrodynamic variables (u, v, w: velocity components in the x-, y-, z-axis respectively, k: turbulence kinetic energy, ε: turbulence kinetic energy dissipation rate).

Plane	Boundary condition
-x	Michelstadt 0°: Inlet: from separate 1D simulation vertical profiles for u, k, ε, v=w=0
	Michelstadt 180°: Outlet: $\frac{\partial \phi}{\partial x}=0$, φ=u, v, w, k, ε
	CUTE: Inlet: from separate 1D simulation vertical profiles for u, v, k, ε, w=0
+x	Michelstadt 0°: Outlet: $\frac{\partial \phi}{\partial x}=0$, φ=u, v, w, k, ε
	Michelstadt 180°: Inlet: from separate 1D simulation vertical profiles for u, k, ε, v=w=0
	CUTE: Outlet: $\frac{\partial \phi}{\partial x}=0$, φ=u, v, w, k, ε
-y	Michelstadt: Symmetry: $\frac{\partial \phi}{\partial y}=0$, φ=*u, v, w, k, ε*
	CUTE: Inlet: from separate 1D simulation vertical profiles for *u, v, k, ε, w*=0

+y	Michelstadt: Symmetry: $\frac{\partial \phi}{\partial y}=0$, ϕ=$u$, v, w, k, ε
	CUTE: Outlet: $\frac{\partial \phi}{\partial y}=0$, ϕ=$u$, v, w, k, ε
Ground	Standard wall functions, roughness length = 0.0625m (Hertwig et al., 2012)
Top	Michelstadt: Fixed values for u, k, ε, $\frac{\partial v}{\partial z}=0$, and w is calculated from the cell mass balance
	CUTE: Fixed values for u, v, k, ε, and w is calculated from the cell mass balance
Building walls	Standard wall functions, roughness length = 0.0625 m (Hertwig et al., 2012)

For Michelstadt, the vertical profiles at the inlet plane (-*x*) for *u*, *k* and *ε* have been constructed based on a separate 1D simulation (in the vertical direction) using the reference velocity U_{ref} = 6 ms^{-1} at the reference height of 99.9 m and neutral stability conditions. For v and w, zero values have been set. The results of the 1-D simulation are presented in Appendix B. The outlet boundary condition at plane +*x* is justified, as this plane is located at a sufficient distance (see above) downwind of the last buildings. For CUTE, the vertical profiles at the inlet planes (-*x* and -*y*) for *u*, *v*, *k* and *ε* have been constructed based on a separate 1D simulation, based on the velocity at 49 m height (6 m/s) and the stability (neutral) as provided by the experiment. For *w*, zero value has been set. The results of the 1D simulations are shown in Appendix B. Outlet boundary conditions at planes +*x* and +*y* have been set, as these planes are located at a sufficient distance downwind of the last buildings.

The wind flow problem was solved as a transient case. The model was allowed to run for a time sufficient to reach a steady-state situation, as revealed by the time-series of velocities obtained at several locations in the domain. The maximum Courant–Friedrichs–Lewy (CFL) number was set equal to 2 based on the authors' experience for numerical stability. The 1st order scheme was used for the time derivative. The 1st order upwind scheme has been used for the approximation of convective terms. The second order central-difference scheme has been used for the approximation of diffusion terms.

4.2. The inverse source term estimation computations

Using the calculated flow field, the transport equation (2) for the adjoint variable *c** has been solved, considering as source the location of each sensor. All available concentration sensors have been used in each dispersion case (see Figure 1 for Michelstadt and Figure 2 for CUTE). Therefore, the adjoint model has been solved as many times as the available concentration sensors in each dispersion case. The transport equation for the adjoint variable has been discretized on the same grid as the flow equations (Table 1). The boundary conditions set for the adjoint variable *c** at each boundary plane or solid surface of the domain are presented in Table . The problem was solved as a transient-in-time case and the solution proceeded until a steady-state situation was reached. For the discretization of the convective term in the adjoint equation the upwind scheme was used. The time step was kept constant and equal to 1 s.

Table 3: Boundary conditions for the adjoint variable *c**.

| -x | $\frac{\partial c^{*}}{\partial x}=0$ |
| +x | $\frac{\partial c^{*}}{\partial x}=0$ |

-y	$\dfrac{\partial c^*}{\partial y} = 0$
+y	$\dfrac{\partial c^*}{\partial y} = 0$
Ground	$\dfrac{\partial c^*}{\partial z} = 0$
Top	$\dfrac{\partial c^*}{\partial z} = 0$
Building walls	$\dfrac{\partial c^*}{\partial s} = 0, \ s{=}x, y, z$

After the calculation of the adjoint variable at all grid points for each concentration sensor location, the next steps were to calculate the source location and emission rate. The source location was estimated by calculating the value of function *J* according to Eq. (1) for each computational cell in the domain and finding its minimum. The centre of the computational cell where the function *J* attained its minimum value has been considered to be the source location. Then the emission rate was calculated by Eq. (3).

5. Results and Discussion

5.1. Validation of the hydrodynamic problem solution

The quality of the flow field simulation has been validated only for the Michelstadt experiment because there are no available flow measurements for CUTE. For the validation, the calculated non-dimensional velocities U/U_{ref} and V/U_{ref} have been compared with the corresponding experimental values.

Similar to Efthimiou et al., (2017) the comparison has been performed using the Hit Rate (*HR*) (Schatzmann et al., 2010). The formal definition of *HR* is the following:

$$HR = \frac{N}{n} = \frac{1}{n}\sum_{i=1}^{n} N_i \ \text{ with } \ N_i = \begin{cases} 1 \, \text{if} \ \left|\dfrac{P_i - O_i}{O_i}\right| \leq D \, \text{or} \, |P_i - O_i| \leq R \\ 0 \, \text{else} \end{cases} \quad (4)$$

where *n* is the total number of compared couples of values, P_i is the model result and O_i is the observation (normalised velocities). In other words, a Hit is added if one of the following conditions is fulfilled:

1. $|P_i - O_i|$ is smaller than the allowed absolute deviation *R*, or
2. $|(P_i - O_i)/O_i|$ is smaller than the allowed fractional deviation *D*

Based on (Hertwig et al., 2012) the proposed values of *R* for the Michelstadt wind tunnel experiment and for each velocity component are *R* = 0.0165 for U/U_{ref} and *R* = 0.0288 for V/U_{ref}. According to the VDI guideline (VDI Guideline, 2005), that structured the application of *HR* metric, the allowed relative difference *D* equals 0.25.

The *HR* obtained for the calculated wind velocity components for the Michelstadt experiment are presented in Table , separately for six groups of sensors, according to their height above ground: a) Sensors which are placed below half the height of the shortest buildings (the shortest buildings are 15 m), b) Sensors which are placed between half the height of the shortest buildings and the height

of roofs of the shortest buildings, c) Sensors which are placed between the height of roofs of the shortest buildings and the height of roofs of the medium buildings (The medium buildings are 18 m), d) Sensors which are placed between the height of roofs of the medium buildings and the height of roofs of the tallest buildings (The tallest buildings are 24 m) e) Sensors which are placed between the height of roofs of the tallest buildings and 48 m (twice the height of the tallest buildings) and f) Sensors which are placed above 48m. It is noticed that the model presents a very good performance above the buildings (z > *24m*), where the *HR* has almost the ideal value (=0.99 and 1.0) for the velocity U/U_{ref} and lower but still high value (=0.75 and 1.0) for the velocity V/U_{ref}. Below the building roofs the *HR* gradually decreases for both velocity components. Below the building roofs V/U_{ref} presents better agreement with the experimental data than U/U_{ref}. Very close to the ground the velocity U/U_{ref} present the lowest *HR* (=0.13). The accuracy of the inverse source term estimation method depends on the accuracy of the flow-field solution as the adjoint equation includes an advection and diffusion term. A systematic study to evaluate this dependency is outside the scope of this paper and is part of the future work planned this framework.

Table 5: *HR* of calculated velocity components of the Michelstadt experiment. The sensors have been grouped according to their height above ground.

Group of sensors	Hit rate (*HR*)	
	U/U_{ref}	V/U_{ref}
48m ≤ z	1.0	1.0
24m ≤ z < 48m	0.99	0.75
18m ≤ z < 24m	0.43	0.41
15m ≤ z < 18m	0.5	0.5
7.5m ≤ z < 15m	0.18	0.33
0m ≤ z < 7.5m	0.13	0.28
Total	0.51	0.51

Scatter plots of calculated vs. measured velocity components U/U_{ref} and V/U_{ref} are presented in Figure , using the same groups of sensors as in Table . It is observed that there is good agreement with the experiment for large velocity magnitudes (i.e., for sensors located above the maximum height of the roofs - 24 m) while for smaller magnitudes (associated with sensors located below the roofs height) the model tends to underestimate the experimental values. At the same time the scatter of the points increases for the lower velocity magnitudes. The underestimation becomes higher as the sensors approach the ground. Nevertheless, the majority of the points lie within the factor-of-2 area, delineated by the dashed lines. These results are similar to the ones presented in Efthimiou et al. (2017).
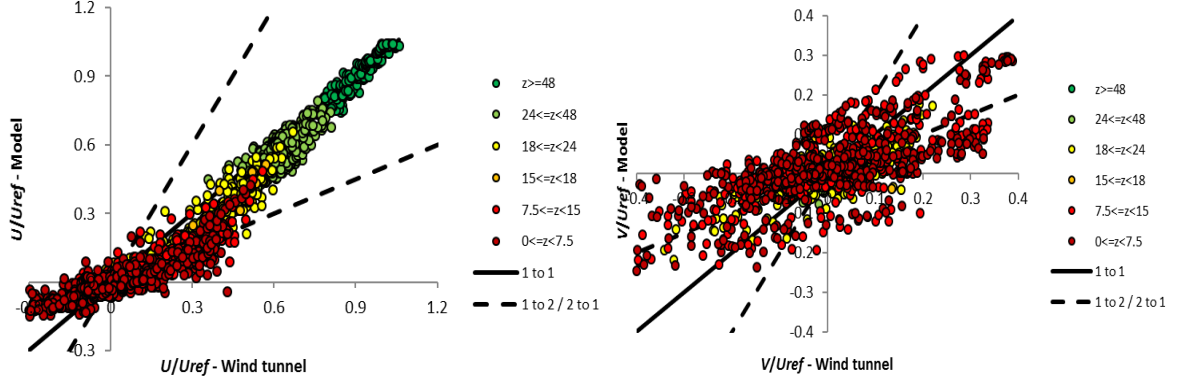
Figure 3: Scatter plots of calculated versus observed velocities *U/Uref* and *V/Uref* at experimental sensors locations; sensors are classified according to their height above ground.

5.3. Source location and emission rate estimation - validation of results

In order to quantify the error in locating the source, the horizontal $r_H = \sqrt{\left(x^s - x_t^s\right)^2 + \left(y^s - y_t^s\right)^2}$

and vertical $r_V = \left| z^s - z_t^s \right|$ distances of the estimated source location (x^s, y^s, z^s) from the true source

location (x_t^s, y_t^s, z_t^s) have been calculated. Concerning the source rate, the relative source rate

ratio $\delta q = \max\left[\left(q^s / q_t^s\right), \left(q_t^s / q^s\right)\right]$ has been calculated which is always greater than unity for both

underestimated and overestimated source rates.

The distances between calculated and actual source location and the emission rate ratios that have been obtained are presented in Table . In this Table, the results of the previous study (Efthimiou et al., 2017) for the MUST experiment are also presented. For Michelstadt experiment, the method presents variable performance. For the horizontal distance, r_H, a satisfactory performance is obtained for cases S4_0°, S5_0°, S6_180° and S7_180°, with the best result achieved for the case S5_0° (r_H = 4.5 m). For the cases S2_0°, S5_180° and S8_180° the horizontal distance between the estimated and the true source location is larger, with the largest obtained for case S8_180° (r_H = 85.50 m). For the vertical distance, r_V, the best performance is achieved for the case S6_180° (r_V = 1.5 m) while the worst for the case S8_180° (r_V = 21.5 m). For the source rate ratio, δq, the best performance is achieved for the case S4_0° and S8_180° (δq = 1.01) while the worst for the case S2_0° (δq = 2.25). No systematic dependence can be observed between the number of sensors and the method's accuracy to estimate the source location or strength. So the performance of the method depends on the characteristics of the source location (open space in the urban area, street canyon perpendicular or parallel to the wind direction, heights of nearest buildings) and the spatial distribution of the sensors in the urban area or in relation to the source. For the CUTE experiment, which is a real urban configuration and therefore more complex than Michelstadt, the method presents a satisfactory performance which indicates its robustness. The method robustness is also indicated by the fact that in all examined cases the method has converged to a —at least acceptable —solution. It is also worth noting that the inverse source term estimation method does not use any prior information regarding the source characteristics.

11

Table 6: Horizontal and vertical distances between estimated and true source locations, and relative source rate ratios for the considered test cases.

Test Case	r_H (m)	r_V (m)	δq (-)	Number of sensors
S2_0^o	62.36	9.5	2.25	57
S4_0^o	13.12	17.5	1.01	25
S5_0^o	4.50	3.5	1.05	22
S5_180^o	72.54	11.5	1.65	35
S6_180^o	9.39	1.5	1.97	38
S7_180^o	8.28	13.5	1.14	117
S8_180^o	85.5	21.5	1.01	58
CUTE	13.69	3.97	1.62	34
MUST (Efthimiou et al., 2017)	1.2	0.1	1.69	244

Each horizontal and vertical distance presented in Table can be divided by the corresponding maximum dimension of the computational domain in the horizontal and vertical directions in order to examine the relative magnitude of the error in the prediction of the source location. The maximum horizontal dimensions of the computational domains for the three experiments were 2094.5 m, 5026.7 m and 361.8 m for Michelstadt, CUTE and MUST, respectively. The vertical dimensions of the computational domains were 144 m, 648 m and 21 m, respectively. The results obtained are presented in Figure . It is clear that in the vertical direction the relative errors in source location are higher than in the horizontal direction. This difference is probably due to that all sensors are located at the same vertical level (near ground). The maximum error in vertical location is equal to 14.93% of the domain height for the S8_180^o case of the Michelstadt experiment. However, the same case presented the best performance for the relative source rate ratio (Table). Also, the best performance for both horizontal and vertical errors is observed for the cases S6_180^o (Michelstadt), CUTE and MUST.
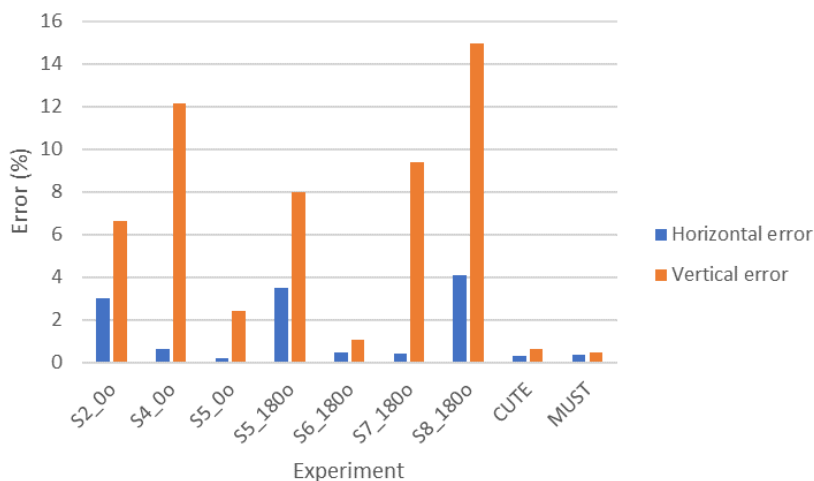

Figure 4: The magnitude of the relative error in the prediction of the source location. Each horizontal and vertical distance presented in Table is divided by the corresponding maximum dimension of the computational domain in the horizontal and vertical direction.

Potential connection of the method's performance with the position of the source was examined. For this reason, two cases have been distinguished: a) the source is located in a street canyon

(MUST, S4_0^o, S5_0^o, S5_180^o, S6_180^o, S7_180^o) and b) the source is located in a more open space (S2_0^o, S8_180^o, CUTE). Figure presents the magnitude of the horizontal error against the experiments. There is a tendency of the first group (the street-canyon-located sources) to present smaller errors than the second group (the open-area-located sources).
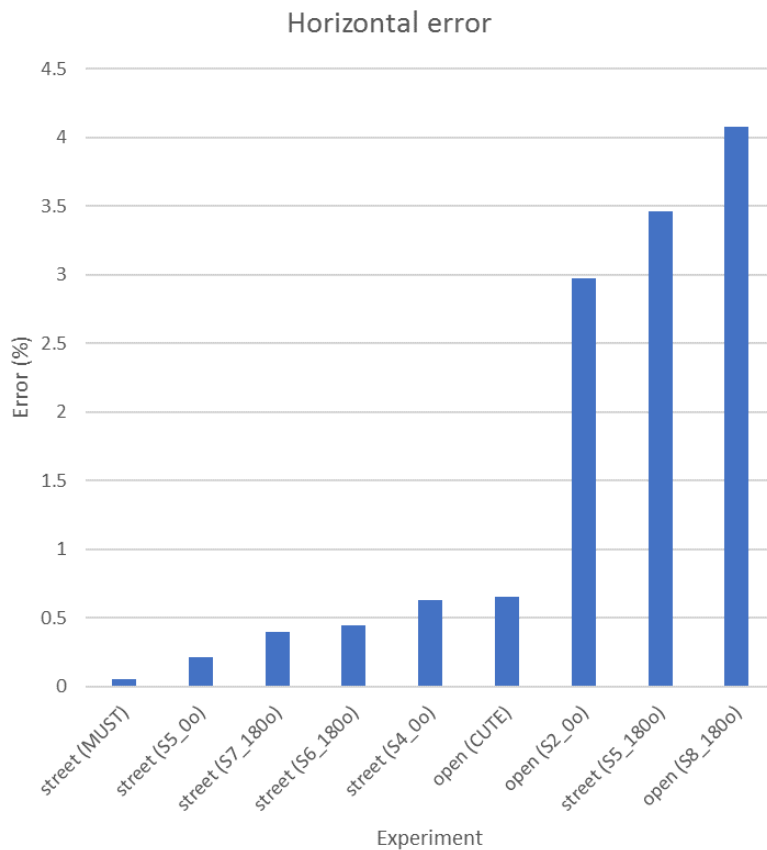

Figure 5: The magnitude of the horizontal relative error of Figure against the two groups of source locations (open-area and street-canyon-located sources).

This can be explained by the fact that the buildings reduce the available space where the source could be located, resulting in a better prediction of the source position. It should be noticed also that the two cases S5_0^o and S5_180^o presented very different performance in locating the source even if it was the same source. This is an indication that the orientation of the street canyon in relation to the incident wind plays also an important role in the performance of the method. Indeed, an additional large eddy simulation of the Michelstadt experiment (Koutsourakis, 2017) has revealed that due to the perpendicular orientation of the street canyon in relation to the wind direction, a spiral vortex is formed along the street canyon. This increases the uncertainty in locating the source inside the canyon.

Figure presents a horizontal plane of CUTE where the heights of the buildings are shown, as well as the real (blue diamond) and the predicted (black cross) sources. It is clear that the performance of the inverse code for this challenging case is very good. The r_H was found equal to 13.69 m.
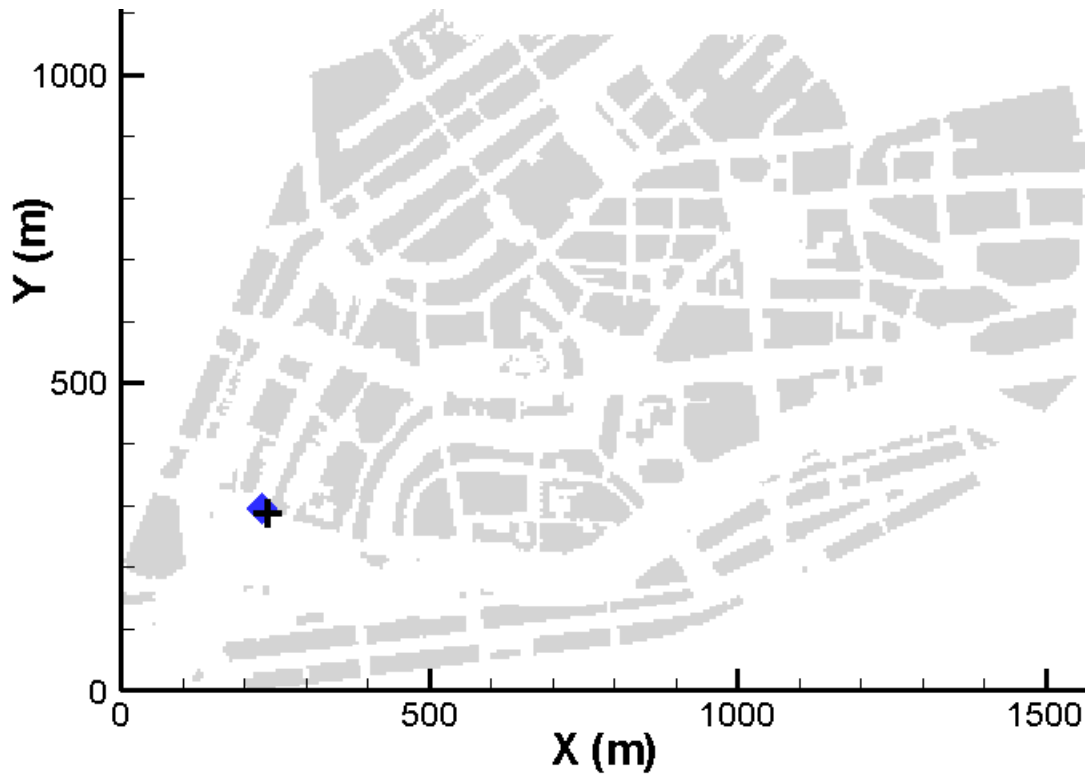
Figure 6: Real (blue diamond) and predicted (black cross) source locations for the CUTE experiment.

6. Conclusions

The work described herein focuses on the validation of an inverse modelling method for estimating the location and emission rate of an unknown point stationary source of passive atmospheric pollutant in a complex urban geometry. The cases studied were two wind tunnel experiments, namely Michelstadt and CUTE, that represent real (or very close to real) urban configurations, in comparison to the less realistic configuration of the MUST experiment that was used in the earlier paper (Efthimiou et al., 2017). The present cases were also more challenging than the MUST experiment because they had less concentration sensors and diverse source locations (open squares, narrow or wide streets, streets aligned perpendicular or parallel to the prevailing large-scale flow, courtyards). The following conclusions can be drawn from the present study:

- The proposed inverse source term estimation method presented a robust behaviour, having converged to a—at least acceptable—solution in all cases, and has resulted in, in most of the cases, a satisfactory determination of the source location (in the vertical and horizontal directions, considering the dimensions of the area of potential source locations and the complexity of the flow situation) and emission rate. The method does not use any prior information regarding the characteristics of the source.
- The performance of the method varies with the examined scenario, even in the same urban geometry, as the simulations of the Michelstadt experiment have revealed. Therefore, the characteristics of the source location are affecting the accuracy of the method, i.e., whether the source is located in a relatively open space inside the urban area, or it is located inside a street canyon that is perpendicular or parallel to the prevailing wind direction, and the heights of the nearest buildings. Based on the results for the Michelstadt experiment, the

14

spatial distribution of the sensors in the urban area and in relation to the source, rather than their number, plays an important role on the accuracy of the source inversion method.

- The error in the horizontal distance varied between 0.05% and 4.1% of the computational domain maximum dimension. The relative source rate ratio varied between 1.01 and 2.25. The vertical distances between estimated and true source locations presented higher errors than the horizontal distances and varied between 0.5% and 14.93% of the computational domain height.
- There appeared to be no correlation between the errors in horizontal distances, vertical distances and release rate.
- The degree of urban complexity is not the factor that most influences the performance of the inverse methodology. Indeed, while the geometry of CUTE is in principle more complex than that of Michelstadt, the source inversion results in case of CUTE were more accurate.

The dependence of the performance of the source inversion method on the accuracy of the calculated wind field will be assessed in a future work by the authors. In this respect it is planned to combine the inverse source term estimation with LES simulations of the flow field, such as those performed by Tolias et al. (2018) for the Michelstadt experiment.

It is finally concluded, that the developed inverse algorithm is appropriate for application in atmospheric dispersion events that involve the detection of a hazardous substance inside an urban area while the location and strength of the emitting source is unknown. The validations presented in this paper increase the confidence that the algorithm can be applied in real urban geometries with a realistic number of available observations. The methodology has a potential for further development to be applicable in a variety of cases, such as emergency response and indoor air quality. Specifically for the method to be applicable for emergency response, the following steps need to be carried out in a preparatory stage, before an actual emergency occurs: set up of the computational domain for the urban area of interest, design of the numerical mesh, computations of the wind flow field for a number of prevailing wind directions (and possibly also for different atmospheric stability categories). If a fixed concentration monitoring network exists, then adjoint computations for the SRFs could also be performed beforehand for each monitoring station and wind field. These results can be stored. At the time of an emergency and based on the particular sensors readings and the actual wind direction, the corresponding SRFs can be retrieved and from these the cost function J (Equation 1) can be calculated. This is a very fast computation that can be performed during an emergency situation and that would give the position of the source. If on the other hand no fixed monitoring station exists, the adjoint computations for the SRFs must be performed at the time of the emergency for the particular measurement stations that would be available. Still these computations can be very fast because they are independent of each other so they can be performed in parallel, with the appropriate hardware infrastructure available. Therefore in any case, the inverse source term estimation method can be considered applicable for emergency response cases, provided that preparatory work has been carried out as described above. A possible challenge in this procedure could be the storage and manipulation of the large volumes of data that would be generated. In this respect the currently available "Big Data" technologies could be exploited.

Appendix A

To assure that the present numerical solutions are grid-independent, a grid-sensitivity analysis has been carried out for the Michelstadt experiment. According to Celik et al. (2008) 3 grids are needed for a grid independency study. Therefore a "fine", a "medium" and a "coarse" grids have been tested, consisting respectively of 28.5, 7.6 and 2.05 million cells, as shown in Table A.1.

The construction of the fine grid started from defining the resolution in the vertical direction. According to the guidelines of COST Action 732, at least 10 cells should be used to describe the height of the buildings. Since the minimum building height in Michelstadt is 15 m, a selection of a minimum cell size in the vertical direction dz_{min}=1m satisfies this requirement. This cell dimension is kept uniform from the ground up and until the maximum buildings height of 24m, so that all buildings have been adequately discretized in the vertical. Above the buildings the vertical cell size increases with a constant ratio of 1.1. In the horizontal directions the minimum cell dimensions that could be used, taking into account the available computational memory resources were $dx_{min}=dy_{min}$=1.5m.

For the medium and coarse grids the same dz_{min}=1m was retained in order not to violate the COST Action 732 guideline. The horizontal resolutions of the medium and coarse grids resulted in using a refinement ratio (Celik et al., 2008) between successive grid resolutions of $r_{32} = r_{21} = 1.55$, where subscript 1 indicates the coarse grid, 2 the medium grid and 3 the fine grid.

In all grids the spatial resolution was kept horizontally uniform inside the urban area (equal to the minimum cell size) and it increased with a constant ratio of 1.1 outside the urban area and moving away from it.

Table A.1: Spatial resolution of the 3 numerical meshes used for the grid sensitivity study for the Michelstadt experiment

Domain dimensions $x/y/z$ (m)	Grid characterization	Total number of cells	Number of cells in each axis			Minimum/maximum cell sizes (m)		
			x	y	z	x	y	z
1800.05/1070.93/144	Fine	28,515,630	935	598	51	1.5/33.97	1.5/12.55	1.0/8.27
	Medium	7,595,838	482	309	51	3.0/35.71	3.0/14.04	1.0/8.27
	Coarse	2,048,160	251	160	51	6.0/37.46	6.0/16.58	1.0/8.27

The flow field was computed by running the CFD model on the three meshes shown in Table A.1. Scatter plots comparing the calculated velocity components, turbulent kinetic energy and dissipation rate of turbulent kinetic energy for the three mesh resolutions are presented in Figure A.1. The

scatter plots reveal a close agreement between medium and fine meshes, indicating that grid independency is attained towards the medium grid resolution.
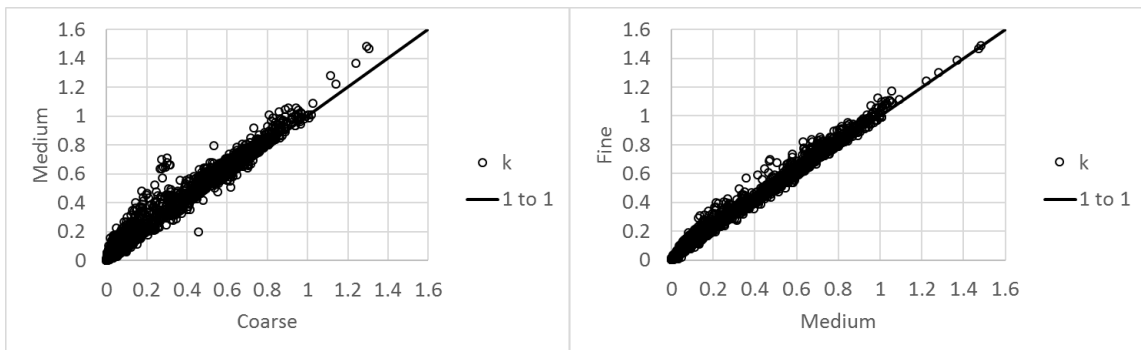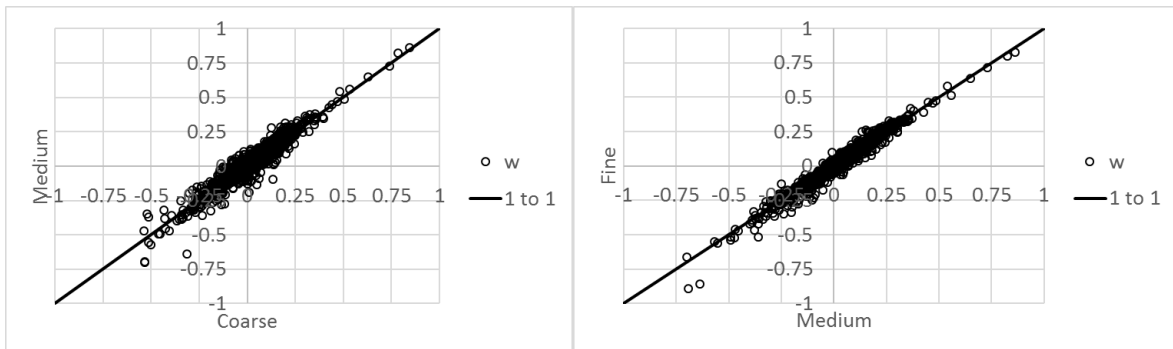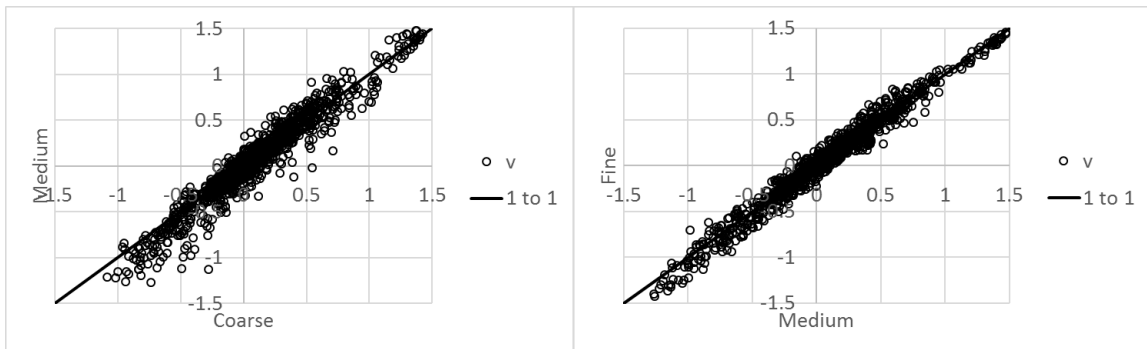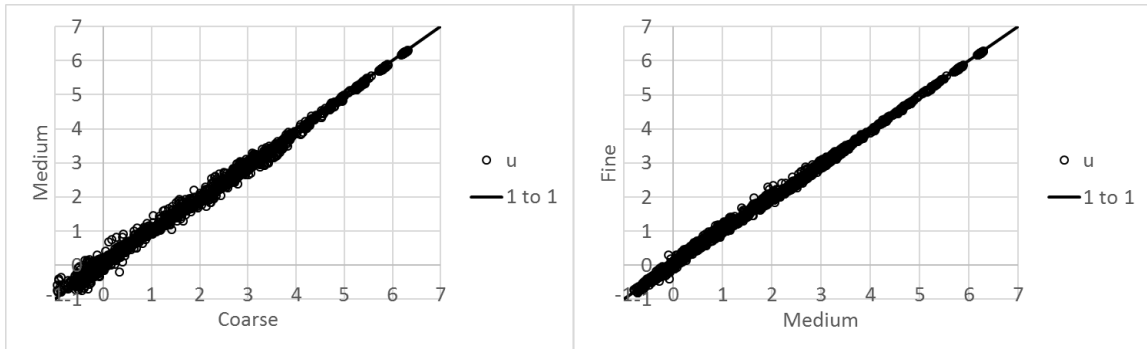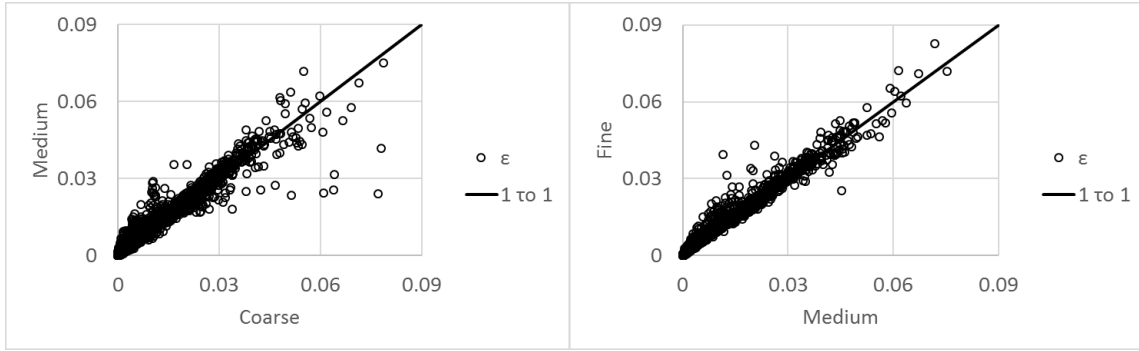
Figure A.1: Comparison of calculated wind velocity components *u*, *v* and *w*, turbulent kinetic energy *k* and dissipation rate *ε*, for the three mesh resolutions. The grid details are presented in Table A.1.

Quantitatively, the level of agreement between the results of two meshes can be expressed through the relative error (RE):

$$RE = \frac{1}{N} \sum_{i=1}^{N} \frac{|o_i - m_i|}{|o_i|}$$

(4)

where "*o*" is always the value of the coarser grid (which is considered as the real value), "*m*" is the value of the finer grid (which is considered as the value that needs to be tested) and "*N*" is the total number of the sensors.

In Table A.2, the relative error between the coarse and medium and between the medium and fine meshes is presented for the different flow variables. Lower values were achieved between the medium and fine grids, in accordance to Figure A.1. Therefore, the medium grid was selected as the basis for all subsequent computations.

Table A.2: Relative error for the calculated wind velocity components *u*, *v* and *w*, turbulent kinetic energy *k* and dissipation rate *ε*, between the three mesh resolutions. The grid details are presented in Table A.I.1.

	Relative Error (*RE*)	
Variable	Coarse-Medium	Medium-Fine
u	0.85	0.32
v	1.27	0.93
w	3.31	1.06
k	1.07	0.28
ε	1.64	0.34
Total	1.63	0.58

Appendix B

One-dimensional flow computations have been performed in this study to define the vertical profiles of the hydrodynamic variables used as inlet boundary condition to the three-dimensional simulations (as in Hertwig et al., 2012, Efthimiou et al., 2018, 2016, 2015).

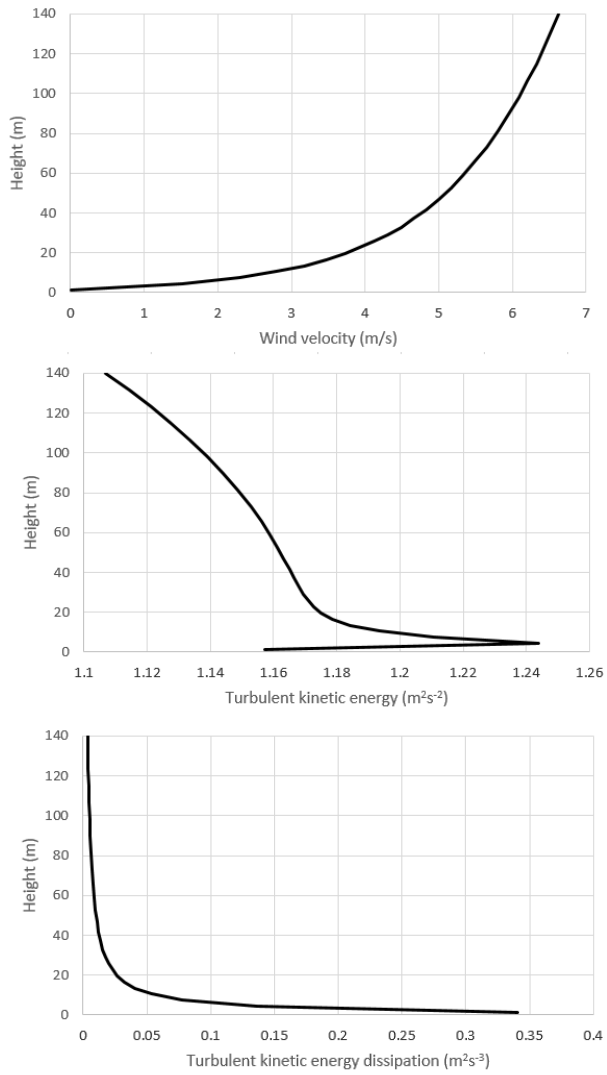The results are presented in Figures B.1 and B.2.

Figure B.1 Calculated 1D profiles of flow variables used as inlet boundary conditions for the 3D simulations of the Michelstadt experiment.
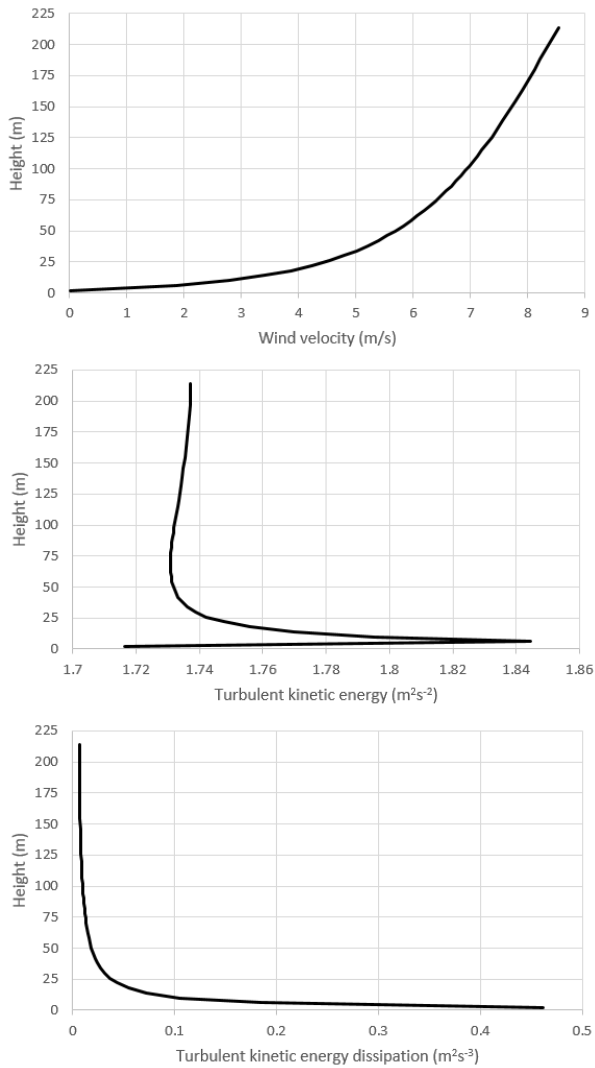
Figure B.2 Calculated 1D profiles of flow variables used as inlet boundary conditions for the 3D simulations of the CUTE experiment.

REFERENCES

Andronopoulos S, Bartzis JG, Würtz J, Asimakopoulos D. Modelling the effects of obstacles on the dispersion of denser-than-air gases. J Haz Mat 1994; 37: 327-352.

Andronopoulos S, Grigoriadis G, Robins A, Venetsanos A, Rafailidis S, Bartzis JG. Three-Dimensional Modelling of Concentration Fluctuations in Complicated Geometry. Environmental Fluid Mechanics 2002; 1: 415–440.

Anspaugh L, Catlin R, Goldman M. The global impact of the Chernobyl reactor accident. Science 1988; 242: 1513-1519.

Argyropoulos CD, Ashraf AM, Markatos NC, Kakosimos KE. Mathematical modelling and computer simulation of toxic gas building infiltration. Process Safety and Environmental Protection 2017; 111: 687-700.

Argyropoulos CD, Christolis MN, Nivolianitou Z, Markatos NC. A hazard identification and parametric analysis of toxic pollutants dispersion from large liquid hydrocarbon fuel-tank fires. M.J. Acosta (Ed.) Advances in Energy Research 2013; 16: Nova Publishers.

Argyropoulos CD, Markatos NC. Recent advances on the numerical modelling of turbulent flows. Appl. Math. Modell. 2015; 39: 693-732.

Argyropoulos CD, Sideris GM, Christolis MN, Nivolianitou Z, Markatos NC. Modelling pollutants dispersion and plume rise from large hydrocarbon tank fires in neutrally stratified atmosphere. Atmos. Environ. 2010; 44: 803-813.

Bartzis JG. ADREA-HF: a three dimensional finite volume code for vapour cloud dispersion in complex terrain. CEC JRC Ispra Report EUR 13580 EN 1991; Ispra: EC Joint Research Centre.

Baumann-Stanzer K, Castelli ST, Stenzel S. COST ES1006 model evaluation case studies: approach and results. University of Hamburg 2015; ISBN: 987-3 9817334-2-6.

Blocken B, Stathopoulos T, Carmeliet J, Hensen JLM. Application of computational fluid dynamics in building performance simulation for the outdoor environment: an overview. Journal of Building Performance Simulation 2011; 4:2: 157-184.

Celik IB, Ghia U, Roache PJ, Freitas CJ, Coleman H, Raad PE. Procedure for estimation and reporting of uncertainty due to discretization in CFD applications. J. Fluids Eng. 2008; 130: 078001-078001-078004.

Chouhan TR. The unfolding of Bhopal disaster. J. Loss Prevent. Proc. Ind. 2005; 18: 205-208.

Chow FK, Kosović B, Chan S. Source inversion for contaminant plume dispersion in urban environments using building-resolving simulations. J. Appl. Meteor. Climato 2008; 47: 1553-1572.

Efthimiou GC, Andronopoulos S, Bartzis JG. Prediction of dosage-based parameters from the puff dispersion of airborne materials in urban environments using the CFD-RANS methodology. Meteorology and Atmospheric Physics 2018; 130(1): 107-124.

Efthimiou GC, Andronopoulos S, Bartzis JG, Berbekar E, Harms F, Leitl B. CFD-RANS prediction of individual exposure from continuous release of hazardous airborne materials in complex urban environments. Journal of Turbulence 2017; 18, 2: 115-137.

Efthimiou GC, Andronopoulos S, Tolias I, Venetsanos A. Prediction of the upper tail of concentration distributions of a continuous point source release in urban environments. Environ. Fluid Mech. 2016; 16: 899-921.

Efthimiou GC, Berbekar E, Harms F, Bartzis JG, Leitl B. Prediction of high concentrations and concentration distribution of a continuous point source release in a semi-idealized urban canopy using CFD-RANS modeling. Atmos. Environ. 2015; 100: 48-56.

Efthimiou GC, Kovalets IV, Venetsanos A, Andronopoulos S, Argyropoulos CD, Kakosimos K. An optimized inverse modelling method for determining the location and strength of a point source releasing airborne material in urban environment. Atmos. Environ. 2017; 170: 118-129.

Elbern H, Schmidt H, Talagrand O, Ebel A. 4D-variational data assimilation with an adjoint air quality model for emission analysis. Environ Modell Softw 2000; 15: 539-548.

Flaherty JE, Stock D, Lamb B. Computational fluid dynamic simulations of plume dispersion in urban Oklahoma City. Journal of Applied Meteorology and Climatology 2007; 46: 2110–2126

Franke J, Hellsten A, Schlünzen H, Carissimo B. Best practice guideline for the CFD simulation of flows in the urban environment. COST Action 732 Quality assurance and improvement of microscale meteorological models 2007; University of Hamburg, ISBN 3-00-018312-4.

Hanna SR, Brown MJ, Camelli FE, Chan ST, Coirier WJ, Hansen OR, Huber AH, Kim S, Reynolds RM. Detailed simulations of atmospheric flow and dispersion in downtown Manhattan. An application of five computational fluid dynamics models. Bulletin of the American Meteorological Society 2006; 87: 1713–1726.

Hertwig D, Efthimiou GC, Bartzis JG, Leitl B. CFD-RANS model validation of turbulent flow in a semi-idealized urban canopy. J. Wind Eng. Ind. Aerod. 2012; 111: 61-72.

Hutchinson M, Oh H, Chen WH. A review of source term estimation methods for atmospheric dispersion events using static or mobile sensors. Information Fusion 2017; 36: 130-148.

Kouichi H, Ngae P, Kumar P, Feiz AA, Bekka N. Optimization of an Urban Monitoring Network for Retrieving an Unknown Point Source Emission. Geoscientific Model Development Discussions 2018, https://doi.org/10.5194/gmd-2018-6.

Koutsourakis N. Personnal Communication 2017.

Kovalets IV, Andronopoulos S, Venetsanos AG, Bartzis JG. (2011) Identification of strength and location of stationary point source of atmospheric pollutant in urban conditions using computational fluid dynamics model. Math Comput Simulat 2011; 82: 244-257.

Kovalets IV, Efthimiou GC, Venetsanos AG, Andronopoulos S, Kakosimos EK, Argyropoulos DC. Inverse identification of an unknown finite-duration air pollutant release from a point source in urban environment. Atmospheric Environment 2018; 181: 82-96.

Lang M, Browne P, Leeuwen PJv, Owens M. Data assimilation in the solar wind: Challenges and first results. Space Weather 2017; n/a-n/a.

Launder BE, Spalding DB. The numerical computation of turbulent flows. Computer Methods in Applied Mechanics and Engineering 1974; 3: 269-289.

Lioy PJ, Laskin JD, Georgopoulos PG. Preparedness and response to chemical and biological threats: the role of exposure science. Ann. N.Y. Acad. Sci. 2016; 1-10.

Ma D, Tan W, Zhang Z, Hu J. Parameter identification for continuous point emission source based on Tikhonov regularization method coupled with particle swarm optimization algorithm. J. Hazard. Mater. 2017; 325: 239-250.

Ma D, Zhang Z. Contaminant dispersion prediction and source estimation with integrated Gaussian-machine learning network model for point source emission in atmosphere. J. Hazard. Mater. 2016; 311: 237-245.

Markatos NC, Christolis M, Argyropoulos C. Mathematical modeling of toxic pollutants dispersion from large tank fires and assessment of acute effects for fire fighters. Int. J. Heat Mass Tran. 2009; 52: 4021-4030.

Mons V, Margheri L, Chassaing JC, Sagaut P. Data assimilation-based reconstruction of urban pollutant release characteristics. J. Wind Eng. Ind. Aerod. 2017; 169: 232-250.

Morita H, Yanagisawa N, Nakajima T, Okudera H, Shimizu M, Hirabayashi H, Nohara M, Midorikawa Y, Mimura S. Sarin poisoning in Matsumoto, Japan. The Lancet 1995; 346; 290-293.

Nivolianitou Z, Argyropoulos CD, Christolis MN, Markatos NC. A methodology for the hazard assessment in large hydrocarbon fuel tanks. Chemical Engineering Transactions 2012; 26: 171-176.

Ohtsuru A, Tanigawa K, Kumagai A, Niwa O, Takamura N, Midorikawa S, Nollet K, Yamashita S, Ohto H, Chhem RK, Clarke M. Nuclear disasters and health: lessons learned, challenges, and proposals. The Lancet 2015; 386: 489-497.

Okumura T, Takasu N, Ishimatsu S, Miyanoki S, Mitsuhashi A, Kumada K, Tanaka K, Hinohara S. Report on 640 Victims of the Tokyo Subway Sarin Attack. Ann. Emerg. Med. 1996; 28: 129-135.

Pocchiari F, Silano V, Zampieri A. Human health effects from accidental release of tetrachlorodibezno-p-dioxin at Seveso, Italy. Ann. N.Y. Acad. Sci. 1979; 320: 311-320.

Pontiggia M, Derudi M, Alba M, Scaioni M, Rota R. Hazardous gas releases in urban areas: Assessment of consequences through CFD modelling. Journal of Hazardous Materials 2010; 176: 589–596.

Rao SK. Source estimation methods for atmospheric dispersion. Atmos. Environ. 2007; 41: 6964-6973.

Robertson L, Langner J. Source function estimate by means of variational data assimilation applied to the ETEX-I tracer experiment. Atmos. Environ. 1998; 32: 4219-4225.

Santiago JL, Dejoan A, Martilli A, Martin F, Pinelli A. Comparison Between Large-Eddy Simulation and Reynolds-Averaged Navier–Stokes Computations for the MUST Field Experiment. Part I: Study of the Flow for an Incident Wind Directed Perpendicularly to the Front Array of Containers. Boundary-Layer Meteorology 2010; 135: 109–132, DOI 10.1007/s10546-010-9466-3.

Schatzmann M, Olesen H, Franke J. COST 732 model evaluation case studies: approach and results. Brussels: COST Office 2010.

Stuart AL, Wilkening DA. Degradation of biological weapons agents in the environment: Implications for terrorism response. Environmental Science & Technology 2005; 39: 2736-2743.

Tolias IC, Koutsourakis N, Hertwig D, Efthimiou GC, Venetsanos AG, Bartzis JG. Large Eddy Simulation study on structure of turbulent flow in a complex city. Journal of Wind Engineering & Industrial Aerodynamics 2018; 177: 101–116.

Trini Castelli S, Tinarelli G, Reisin TG. Comparison of atmospheric modelling systems simulating the flow, turbulence and dispersion at the microscale within obstacles. Environ Fluid Mech 2017; 17: 879–901.

VDI Guideline. Environmental meteorology—Prognostic microscale wind field models—Evaluation for flow around buildings and obstacles. 2005.

Venetsanos AG, Papanikolaou E, Bartzis JG. The ADREA-HF CFD code for consequence assessment of hydrogen applications. Int J Hydrogen Energy 2010; 35: 3908– 3918.

Wang Y, Huang H, Huang L, Ristic B. Evaluation of Bayesian source estimation methods with Prairie Grass observations and Gaussian plume model: A comparison of likelihood functions and distance measures. Atmos. Environ. 2017; 152: 519-530.

Wang BC, Yee E, Lien FS. Numerical study of dispersing pollutant clouds in a built-up environment. International Journal of Heat and Fluid Flow 2009; 30: 3–19

Xue F, Li X, Ooka R, Kikumoto H, Zhang W. Turbulent Schmidt number for source term estimation using Bayesian inference. Building and Environment 2017; 125: 414-422.

Zhang X, Raskob W, Landman C, Trybushnyi D, Li Y. Sequential multi-nuclide emission rate estimation method based on gamma dose rate measurement for nuclear emergency management. J. Hazard. Mater. 2017; 325: 288-300.

Zheng DQ, Leung JKC, Lee BY, Lam HY. Data assimilation in the atmospheric dispersion model for nuclear accident assessments. Atmos. Environ. 2007; 41: 2438-2446.